Robust, Ultrathin, and Highly Sensitive Reduced Graphene Oxide/ Silk Fibroin Wearable Sensors Responded to Temperature and Humidity for Physiological Detection

Hyeonho Cho,[§] Chanui Lee,[§] ChaBum Lee, Sangmin Lee, and Sunghan Kim*

Cite This: Biomacromolecules 2023, 24, 2606−2617

Read Online

ACCESS | 📊 Metrics & More | 📰 Article Recommendations | 🆂🆘 Supporting Information

ABSTRACT: Skin temperature and skin humidity are used for monitoring physiological processes, such as respiration. Despite advances in wearable temperature and humidity sensors, the fabrication of a durable and sensitive sensor for practical uses continues to pose a challenge. Here, we developed a durable, sensitive, and wearable temperature and humidity sensor. A reduced graphene oxide (rGO)/silk fibroin (SF) sensor was fabricated by employing a layer-by-layer technique and thermal reduction treatment. Compared with rGO, the elastic bending modulus of rGO/SF could be increased by up to 232%. Furthermore, an evaluation of the performance of an rGO/SF sensor showed that it had outstanding robustness: it could withstand repeatedly applied temperature and humidity loads and repeated bending. The developed rGO/SF sensor is promising for practical applications in healthcare and biomedical monitoring.
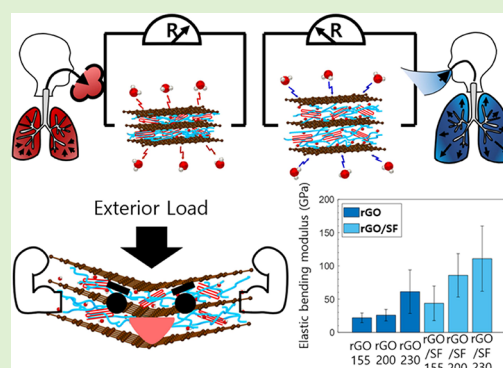
1. INTRODUCTION

The skin's temperature and humidity are representative parameters used for monitoring physiological processes and conditions such as respiration, fever, and perspiration.[1−3] While real-time continuous monitoring of physiological signals is important for doctors to comprehensively understand a patient's condition, traditional methods for detecting the body's condition, such as the use of thermometers, cannot provide continuous information. For real-time detection of physiological signals, a wearable sensor can be used, and many wearable temperature and humidity sensors have been developed.[4−7] In particular, wearable sensors based on biomaterials, such as mycelium and cellulose, have been developed to detect various environmental conditions such as humidity.[8−10]

Reduced graphene oxide (rGO) is one of the materials favored for use as a temperature and humidity sensor, owing to its rich oxygen-containing functional groups, high electrical conductivity, and good thermal properties.[11−14] The oxygen-containing functional groups, such as hydroxyl, epoxy, and carboxyl groups, are responsible for its hydrophilic nature.[15,16] Notably, rGO-based materials can be used as temperature sensors in a wide temperature range owing to their high electrical conductivity and good thermal properties.[17,18] However, the development of an rGO-based sensor with superior mechanical properties, a facile fabrication process, and high sensitivity poses a challenge.

An rGO film is easily delaminated because of its low interfacial strength and brittle nature, and hence, it is not suitable for practical use.[19,20] Recently, silk proteins, which are biomaterials, have been found to have the potential to be used in carbon-based sensors for physiological monitoring.[21−23] In particular, the addition of silk fibroin (SF), which is a silk protein and which can interact strongly with rGO flakes through hydrogen bonding, polar−polar bonding, and hydrophobic−hydrophobic bonding, can prevent delamination and enhance the flexibility of rGO films.[24] An rGO/SF composite with a nacre-like structure can be prepared by a layer-by-layer (LbL) self-assembly method.[25,26] This method is facile and can be used to obtain composites with mechanical properties superior to those of rGO. Nacre is 1000 times tougher than its constituents because of strong interfacial interaction between its constituents, which results from its brick-and-mortar structure.[27−30] Because of its nacre-like structure, a GO−SF composite prepared by an LbL method has higher strength and toughness than one prepared using a simple mixing and casting method.[24,31,32] Xu et al. prepared a GO−SF composite with high mechanical properties (elastic modulus: 145 GPa; tensile strength: 300 MPa) by using a spin-assisted LbL method.[16] By contrast, a GO-SF composite prepared by Huang et al. by simply mixing a GO solution and an SF solution and casting
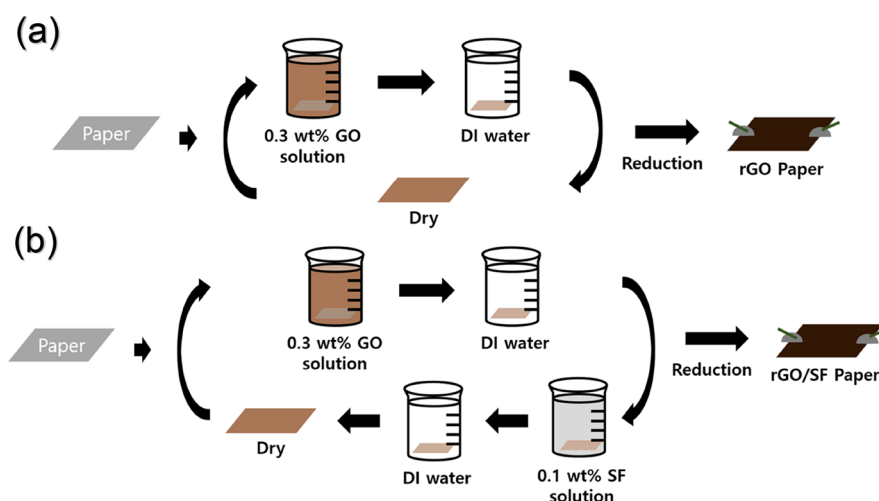
Scheme 1. Schematics of the Fabrication Process of (a) rGO Paper and (b) rGO/SF Paper

the solution at room temperature had a tensile modulus of 17.2 GPa and a tensile strength of 221 MPa.[27] These results showed that LbL fabrication methods can enhance the overall mechanical properties of GO/SF and rGO/SF materials. In particular, the mechanical properties of rGO can be adjusted by controlling the defect content.[33,34] Several methods, such as dip, spin, spray, electromagnetic, and fluidic coating, have been used to fabricate LbL structures.[35,36] The LbL dip-coating technique for fabricating a nacre-like structure with nanoscale thickness is facile and cost-effective. To the best of our knowledge, researchers have elucidated the sensing mechanism of rGO-based temperature sensors: an increase in the temperature leads to increased charge transport because of enhanced hopping and tunneling effect.[37−39] Furthermore, studies have shown that the rGO structure exhibits negative thermal expansion (NTE).[40] The rGO network connection changes with the temperature because of this NTE, resulting in changes in electrical parameters such as resistance and current of the rGO structure. However, there are few studies on the effect of physical changes in the rGO structure on the electrical signals.

Although GO-based humidity sensors show good performance, rGO-based humidity sensors are more advantageous.[41,42] Owing to its hydrophilic properties resulting from the abundance of oxygen-containing functional groups, GO swells or shrinks when the humidity changes. However, because GO has low electrical conductance, measuring the electrical signal of a GO humidity sensor is difficult. Hence, GO should be combined with other conductive materials for realizing a humidity sensor with high sensitivity.[43,44] On the other hand, owing to its high electrical conductance and hydrophilic surface functional groups, rGO has the potential to be used as a temperature and humidity sensor. To use GO as a low-electrical-conductance humidity sensor, we should use the capacitance change rather than the resistance change to detect humidity changes. However, a capacitive-signal-based humidity sensor has a complex structure, unlike a resistive-signal-based humidity sensor, which has a single conductive layer as the sensing layer.[41,45,46] Furthermore, since the number of functional groups in rGO is tailorable, the performance of an rGO sensor can be adjusted by varying the number of functional groups, which would influence the interaction of the sensor with moisture in the air.[47,48] Since SF has low electrical

conductance, the advantage of rGO/SF-based sensors over GO/SF-based sensors can be attributed to the rGO/SF composite's significantly improved electrical conductance owing to rGO.

Here, we developed an rGO/SF multifunctional sensor with superior mechanical properties by using a facile LbL dip-coating technique and thermal reduction treatment. The mechanical properties of the rGO/SF sensor were determined by conducting the atomic force microscope (AFM) bending test. The rGO/SF sensor was found to have superior mechanical properties because of the strong hierarchical interaction between rGO and SF. The elastic bending modulus of an rGO/SF film could be enhanced by up to 232% compared with that of an rGO film. Furthermore, the mechanical properties of rGO/SF films could be tailored by adjusting the reduction temperature since (1) the number of defects in the rGO lattice structure varies with the temperature and (2) SF can be recrystallized. The sensing mechanism of the rGO/SF sensor was that its structure varied with the amount of moisture adsorbed and temperature. When the temperature and humidity of the rGO/SF sensor's environment changed, the interaction between the adsorbed moisture and rGO flakes altered the rGO networking in the sensor, which caused the electrical conductance of the sensor to change. The sensitivity of the rGO/SF sensor could be tailored by varying the number of hydrophilic functional groups in the rGO flakes, which caused the degree of moisture−rGO flake interaction to change. The sensitivity of the humidity and temperature sensor decreased with an increase in the reduction temperature. The sensitivity changes of the sensors are attributed to changes in its structure, which can be monitored by temperature coefficient of resistance (TCR). The TCR of the rGO/SF sensor was adjusted to 2.20, 1.87, 1.73, 1.66, 1.50, and 1.39% K^{-1} for reduction temperatures of 155, 170, 185, 200, 215, and 230 °C, respectively. To evaluate the stability and durability of the temperature and humidity sensor, we performed a cyclic test for 1000 cycles. The rGO/SF sensor showed excellent stability and durability. Although its performance in terms of parameters such as the TCR slightly deteriorated, its outstanding durability resulted in high robustness to repeated temperature and humidity loads and repeated bending, without any degradation of the sensing performance. Since the developed rGO/SF sensor can be used

for monitoring physiological parameters and processes such as respiration and skin temperature, it has the potential to be used in practical applications in the fields of healthcare and biomedical monitoring.

2. EXPERIMENTAL DETAILS

2.1. Material Preparation. *2.1.1. Preparation of GO and SF.* GO was prepared by the well-established Hummer's method.[49] Briefly, graphite power (0.8 g) was oxidized and then exfoliated using sodium nitrate (0.4 g), sulfuric acid (18.5 mL), and potassium permanganate (2.4 g) for 3 h in an ice bath. The oxidized and exfoliated graphite solution was then placed in a water bath and stirred for 1 h. Deionized (DI) water (37.5 mL) was added dropwise very slowly to the solution, and the solution was boiled in the water bath that was maintained at approximately 90 °C for 2 h. The solution was then cooled in air, and DI water (112.5 mL) was added to it under stirring for 1 h. Next, hydrogen peroxide (30%, 12.5 mL) was added very slowly to the solution, and the solution was then sealed with aluminum foil and stirred for 1 h. The resulting solution was precipitated for more than 6 h. The supernatant of the solution was replaced with new DI water, and the solution was precipitated again. The replacement with DI water and precipitation were repeated twice, and the solution was subsequently filtered by using a vacuum filtration system and 1 μm filter paper. Finally, GO was obtained by drying the filter paper at 60 °C.

Aqueous SF solution was prepared from *Bombyx mori* cocoons.[50] Briefly, silk cocoons (5 g) were degummed by immersing them in boiling sodium carbonate solution (0.02 M) for 30 min. They were then squeezed and washed with DI water. The degumming and washing processes were repeated thrice. Subsequently, the silk cocoons were dried in a fume hood for 12 h and then dissolved in lithium bromide (9.3 M) at 60 °C in an oven for 4 h. The silk solution was repeatedly dialyzed by using a hydrated dialysis cassette (3500 MW cutoff), and it was then repeatedly refined through centrifugation (9000 rpm, 20 min). The SF solution that was finally obtained was stored in a refrigerator at 4 °C.

2.1.2. Preparation of the Temperature Sensor (rGO and rGO/SF). An rGO-based temperature sensor was prepared as follows (Scheme 1). An office paper was cut to have dimensions of 1 cm × 3 cm. GO paper was prepared by LbL dip-coating the paper with GO aqueous suspension (0.3 wt %), and GO/SF paper was prepared by LbL dip-coating an office paper alternately with GO aqueous suspension (0.3 wt %) and SF solution (0.1 wt %). Next, the two papers (GO and GO/SF papers) were washed by immersing each of them in DI water to remove the excess GO coating, and they were dried at 60 °C in an oven for 30 min. The LbL dip-coating process was repeated until the desired number of bilayers was formed (generally three bilayers). Thereafter, the GO and GO/SF papers were thermally reduced at 155, 170, 185, 200, 215, and 230 °C in an oven for 3 h. For the measurement of electrical signals of the thermal reduced GO and GO/SF (hereafter referred to as rGO and rGO/SF) sensors, electrical wires were attached to the ends of the rGO and rGO/SF sensors using a silver paste adhesive (P-100, CANS). The distance between electrodes (i.e., the wires at the two ends of the rGO and rGO/SF sensors) was approximately 2.3 cm.

2.2. Method. *2.2.1. Characterization of rGO and rGO/SF Films.* The morphology of rGO and rGO/SF films was observed using AFM. The soft tapping mode was used to obtain morphological images with a NANOSENSORS tip (PPP-NCHR), and the scan rate was 0.5 Hz. According to manufacturer specifications, the tip had a force constant of 42 N/m and a radius below 10 nm. The chemical analysis of the rGO and rGO/SF films was conducted using field emission scanning electron microscopy (FE-SEM; SIGMA, Carl Zeiss) and energy-dispersive X-ray spectrometry (EDS) at an accelerating voltage of 15 kV. The Fourier transform infrared (FTIR) spectra of the rGO/SF films obtained at reduction temperatures of 155, 200, and 230 °C was recorded using an FTIR spectrometer (Nicolet 6700, Thermo Scientific).

2.2.2. Characterization of Sensors. The performance of the rGO and rGO/SF sensors as temperature sensors and humidity sensors was evaluated. The performance of a temperature sensor was evaluated by placing it on a hot plate and measuring the sensor's temperature (Figure S1a) with a thermometer (FLUKE 52 II, FLUKE) at different hot plate temperatures. The temperature range was 30−100 °C. The performance of a humidity sensor was evaluated by using saturated salt solutions, namely, LiCl, MgCl$_2$, NaCl, and K$_2$SO$_4$, that could control the relative humidity at 11, 33, 75, and 97%, respectively (Figure S1b). The sensor was placed in a closed humidity-controlled vessel containing the desired saturated salt solution, and a hygrometer (DHT22, Arduino) was used to measure the relative humidity. While measuring the temperature and relative humidity of a sensor's environment, a source meter (Keithley 2450, Keithley Instruments) was used to measure the electrical signals of the sensors.

2.2.3. AFM Bending Test. The AFM bending test was performed to determine the mechanical properties of the rGO and rGO/SF films; AFM (NX-10, Park Systems) was used in the test. The rGO and rGO/SF films were prepared on a silicon (Si) wafer (100 mm diameter) by using an LbL dip-coating method (Scheme 1). The wafer was spin-coated to form a sacrificial layer of cellulose acetate (CA). Before the AFM bending test, the rGO and rGO/SF films were transferred on a copper mesh grid after removing the CA layer with acetone solution. During the AFM bending test, an AFM cantilever (HQ:XSC11, MikroMasch) with a spring constant of 0.2 N/m was used, and the z-scanner speed was 0.1 μm/s. The AFM bending test specimen was prepared by using an LbL dip-coating method similar to that used for the sensor.

3. RESULTS AND DISCUSSION

3.1. Fabrication of rGO and rGO/SF Films. The rGO and rGO/SF films were prepared using an LbL dip-coating method and thermal reduction treatment (Scheme 1), and their morphologies were observed using FE-SEM (Figure 1a). For all reduction temperatures, the rGO and rGO/SF films were well coated on papers. EDS analysis was performed to determine the effect of the reduction temperature on the chemical properties of the films. For both films, the carbon to oxygen (C/O) ratio increased with the reduction temperature
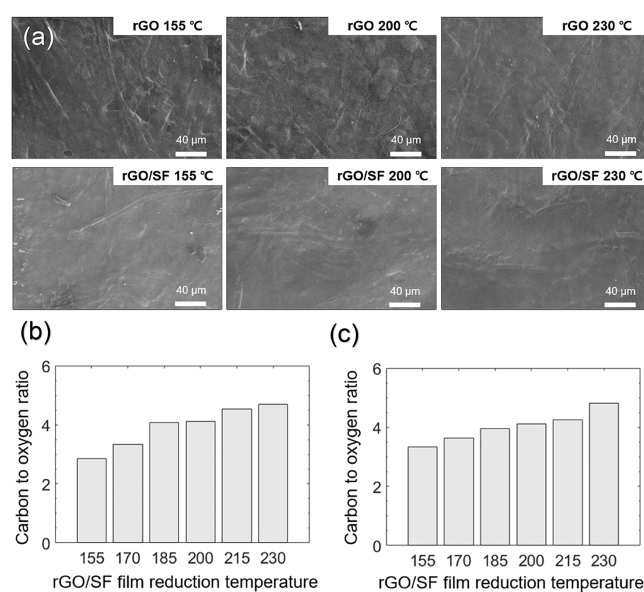

Figure 1. (a) FE-SEM images showing morphologies of rGO and rGO/SF films. The carbon to oxygen (C/O) ratio of (b) rGO and (c) rGO/SF films determined using the EDS. All scale bars are 40 μm.

(Figure 1b,c). This increase in the C/O ratio was attributed to a decrease in the number of oxygen groups of GO with an increase in the reduction temperature.[51] The tailorable C/O ratio allowed for the interaction of the rGO and rGO/SF films with various materials (such as moisture) to be engineered. An increase in the C/O ratio of the films increased their electrical conductivity (Figure S2). Representative EDS results for rGO and rGO/SF films for a reduction temperature of 230 °C are shown in Figure S3. Since the thin films were on a Si wafer, the intensity of the Si peak in the EDS results was large. However, despite the large intensity of the Si peak, the carbon and oxygen peaks could be clearly discerned.

3.2. Mechanical Properties of rGO and rGO/SF Films.
The overall mechanical properties of LbL films were influenced by the interfacial interaction between layers.[52−55] For the accurate determination of the mechanical properties of rGO and rGO/SF films with abundant interfacial interactions between layers, the films were prepared using a spin-assisted LbL technique.[52,56] The mechanical properties were investigated using the AFM bending test.[57] The rGO and rGO/SF films were transferred on an aperture grid to perform the test. Before the test, the surface of the film was scanned using the AFM to determine the aperture (Figure S4). The location of the aperture grid supporting the films was determined from a force image and a morphological image of the films.

The AFM bending test was conducted at the center of a hole, which was identified from an AFM image. The AFM tip approached the film at the center of the hole and indented the film. While the AFM tip caused the bending of the film, the AFM cantilever was also bent by the reaction force associated with the bending of the film. Considering the deflection of the AFM cantilever (δ), we expressed the deflection of the film (w) as[57]

$$w = \Delta z - \delta \tag{1}$$

where Δz is the distance of the z-scanner between the instants when the AFM tip came in contact with the film (with no deflection of the AFM cantilever) and when the film was bent by the AFM tip. Because the deflection of the AFM cantilever (δ) and the distance of the z-scanner (Δz) were easily obtained from AFM system, the deflection of the film (w) could be calculated from eq 1. Figure S5 shows the force−displacement (Δz) curves (FD curves) for an rGO film and an rGO/SF film obtained from AFM bending tests. The continuous FD curves show the absence of delamination and damage during the AFM bending test. Since the rGO and rGO/SF films were immersed in acetone solution during their transfer from an Si wafer to a copper mesh grid, a residual stress could have been generated after the evaporation of the acetone solution. The absence of residual stress was shown by applying a force in the opposite direction (Figure S6c; retracting direction) to the rGO and rGO/SF films during the AFM bending test; the load−deflection curves in cases of approaching and retracting were almost identical for the opposite force in the AFM bending test (Figure S6).

From AFM bending tests, load−deflection plots were obtained for the rGO and rGO/SF films for reduction temperatures of 155, 200, and 230 °C (Figure 2a). For both types of films, the slope of the load−deflection curves decreased with an increase in the reduction temperature. The thicknesses of the rGO and rGO/SF films used in the AFM bending tests were obtained to determine the mechanical properties of the films (Figure 2b). The thicknesses of the rGO
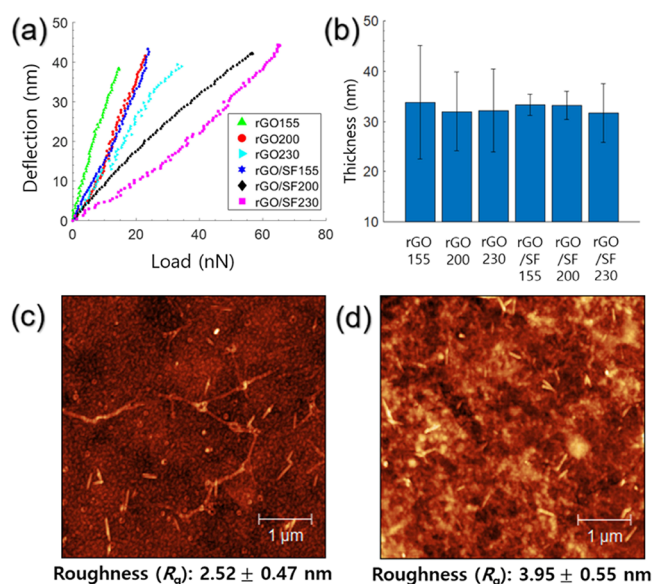

Figure 2. AFM load−deflection plots of (a) rGO and rGO/SF sensors. (b) Thickness of different types of bilayer films. Morphological AFM images of (c) rGO and (d) rGO/SF sensors for a reduction temperature of 200 °C.

film for reduction temperatures of 155, 200, and 230 °C were 33.8, 32.0, and 32.1 nm, respectively, and the thicknesses of the rGO/SF film for these reduction temperatures were 33.3, 33.2, and 31.7 nm, respectively. The thicknesses of all films were very similar. The root mean square (RMS) roughness of the rGO and rGO/SF films for the reduction temperature of 200 °C was obtained as 2.52 and 3.95 nm, respectively. These values indicated that the surface of the films used in the AFM bending test was sufficiently flat (Figures 2c,d and S7).[57,58]

The reciprocal of the slope of the load−deflection plots was defined as the effective bending stiffness.[59] The effective bending stiffness values of the rGO film were 0.43, 0.71, and 1.04 N/m for reduction temperatures of 155, 200, and 230 °C, respectively (Figure 3a), and the parameter's values for the rGO/SF film were 0.83, 1.61, and 1.81 N/m for these reduction temperatures, respectively. The effective bending stiffness of both types of films increased with the reduction temperature. In particular, for a given reduction temperature, the effective bending stiffness of the rGO film was less than that of the rGO/SF film. Since the thicknesses of the rGO and rGO/SF films were very similar, it was apparent that compared with the rGO film, the rGO/SF film showed enhanced mechanical properties.

The elastic bending modulus of the rGO and rGO/SF films for reduction temperatures of 155, 200, and 230 °C was calculated from the following expression:[57]

$$E_{\text{bending}} = \frac{12(1 - v^2)}{t^3} \frac{2r^2 \ln(r/a) + (a^2 - r^2)}{16\pi} \frac{P}{w} \tag{2}$$

where t is the film thickness, v is Poisson's ratio (assumed as 0.3), r is the distance between the loading point in the AFM bending test and the center of the aperture grid, P is the force applied to the film, w is the deflection of the film, and a is the aperture of the grid. Because the AFM bending test was conducted at the center of the aperture grid, r was set to zero. The thickness (t) obtained from Figure 2b was used to calculate the elastic bending modulus. From eq 2, the elastic
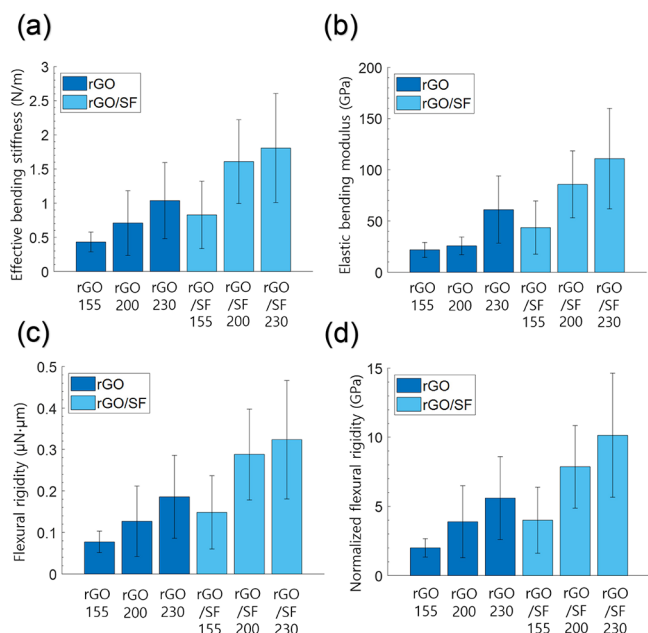
Figure 3. Calculated values of the (a) effective bending stiffness, (b) elastic bending modulus, (c) flexural rigidity, and (d) normalized flexural rigidity of rGO and rGO/SF sensors for reduction temperatures of 155, 200, and 230 °C.

Figure 4. Schematic of the process by which a nacre-like rGO/SF structure is formed from a GO/SF structure.

bending modulus of the rGO film for reduction temperatures of 155, 200, and 230 °C was calculated to be 21.9 ± 7.3, 25.8 ± 8.6, and 61.1 ± 32.8 GPa, respectively, and that of the rGO/SF film for these reduction temperatures was 43.7 ± 26.0, 85.8 ± 32.7, and 110.9 ± 49.0 GPa, respectively (Figure 3b). The elastic bending modulus of both types of films increased with the reduction temperature. Notably, compared with the rGO film, the rGO/SF film's elastic bending modulus was enhanced by 99.5, 232.6, and 81.5% for reduction temperatures of 155, 200, and 230 °C, respectively.

Flexural rigidity and normalized flexural rigidity are important mechanical properties that provide useful information in the design of wearable devices. Flexural rigidity can be calculated as[57]

$$D = \frac{P}{16\pi w}\left(2r^2\ln\frac{r}{a} + a^2 - r^2\right) \tag{3}$$

where P/w is the effective bending stiffness. The calculated flexural rigidity of the rGO film for reduction temperatures of 155, 200, and 230 °C was 0.08, 0.13, and 0.19 μN·μm, respectively, and for the rGO/SF film, the values were 0.15, 0.29, and 0.32 μN·μm at these reduction temperatures, respectively (Figure 3c). The normalized flexural rigidity (D/t^3) of the rGO film was calculated to be to 2.00, 3.89, and 5.60 GPa for reduction temperatures of 155, 200, and 230 °C, respectively, and for the rGO/SF film, the values at these reduction temperatures were 4.00, 7.86, and 10.15 GPa, respectively (Figure 3d). The enhanced flexural mechanical properties of the rGO/SF film indicate that the film will show more robust performance than the rGO film when used as a sensor.

The enhanced mechanical properties of the rGO/SF film were attributed to its nacre-like structure (Figure 4). In particular, the rGO and SF layers can interact strongly through polar–polar, hydrophobic, and hydrogen bonding interactions.[58,60] The mechanical properties of an rGO film can be
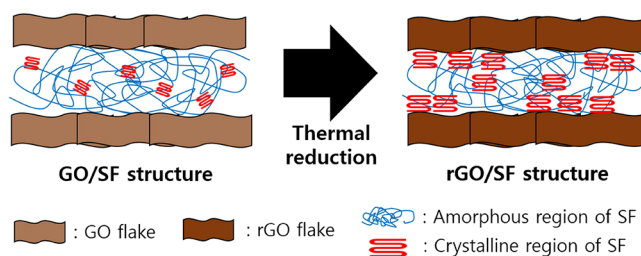
enhanced by adding SF layers because of the interaction between the film and SF layers.[57] The enhanced mechanical properties at a high reduction temperature was attributed to the reduction in the number of defects in the lattice structure of an rGO flake.[61,62] Because the number of defects in the lattice structure of an rGO flake decreased with an increase in the reduction temperature, the mechanical properties of rGO/SF films were enhanced to a greater extent for a higher reduction temperature.[63,64]

The secondary structure of SF was changed by the thermal reduction treatment, and this led to a change in the mechanical properties of the rGO/SF film.[65,66] The amorphous region of SF can be transformed into a crystalline region (β-sheet) through high temperature reduction treatment. Since the β-sheet can strongly interact with a hydrophobic part of rGO, the β-sheet formed at the interface between SF and rGO was strongly bound to the adjacent rGO layers (Figure 4).[60] The strong binding between the β-sheet and adjacent rGO layers increased the interfacial shear strength and thereby enhanced the mechanical properties of the rGO/SF film.[60] The increased number of β-sheet could be monitored by using FTIR spectra of rGO/SF films obtained at reduction temperatures of 155, 200, and 230 °C (Figure S8). Owing to its enhanced mechanical properties and the change in its secondary structure after thermal reduction treatment, the rGO/SF film can provide robust performance when used as a sensor.

An rGO/SF film with a structure that was not nacre-like was prepared to compare it with an rGO/SF film with a nacre-like structure. The former rGO/SF film was fabricated by mixing rGO and SF solutions and dip-coating the resulting solution on a Si wafer. The morphology of rGO/SF films with and without a nacre-like structure was investigated by using a scanning AFM tip (Figure S9a,b). The surface of the rGO/SF film whose structure was not nacre-like was rough. On the other hand, the surface of the rGO/SF film with a nacre-like structure was smooth, which implied alternately stacked rGO and SF layers; both the rGO and SF films had a smooth and uniform surface (Figure S9c,d). A nacre-like structure can transfer stress from one location to the surrounding regions and thereby dissipate stress.[67] Accordingly, the mechanical properties of an rGO/SF film with a nacre-like structure can be enhanced, unlike an rGO/SF film with a structure that is not nacre-like.

3.2.1. Performance of rGO and rGO/SF Sensors. We evaluated the rGO and rGO/SF temperature-humidity sensors by heating them and measuring their electrical signals and temperature with a source meter and thermometer, respectively (Figure S1a). The normalized resistance ($\Delta R/R_0$) of both sensors decreased with an increase in their temperature (Figure 5a). Furthermore, the normalized resistance of both sensors was more strongly affected by the temperature for a
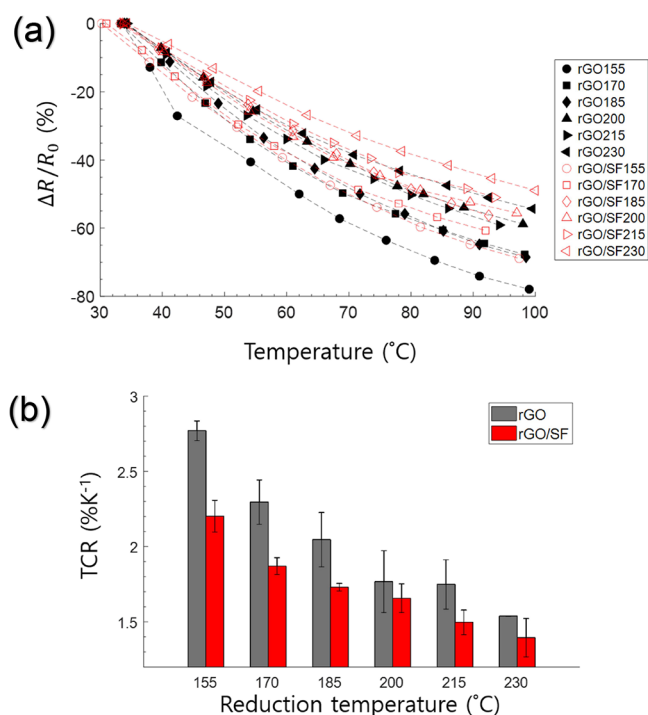
Figure 5. (a) Variation of the responsivity of rGO and rGO/SF temperature sensors (prepared at different reduction temperatures) in terms of resistance change, $\Delta R/R_0$, as a function of the temperature. (b) Variation of the TCR at 300 K with the reduction temperature for the rGO and rGO/SF sensors.

lower reduction temperature. Thus, both rGO and rGO/SF films have the potential to be used as temperature sensors with tunable performance.

The relationship between the resistance and the temperature of a sensor is expressed by the following Arrhenius-type equation:[68]

$$R = R_0 \exp\left(-\frac{E_a}{kT}\right) \tag{4}$$

where R is the resistance of the sensor, R_0 is initial resistance of the sensor, T is the temperature of the sensor, E_a is the activation energy, and k is the Boltzmann constant. All the rGO and rGO/SF sensors, irrespective of the reduction temperature, were well fitted by eq 4 (Figures S10 and S11). The TCR of the rGO and rGO/SF sensors was calculated from the equation[68]

$$\text{TCR} = \frac{dR}{dT}\frac{1}{R} \tag{5}$$

From eqs 4 and 5, the TCR of the rGO sensor was obtained to be 2.77, 2.30, 2.05, 1.77, 1.75, and 1.54%/K for reduction temperatures of 155, 170, 185, 200, 215, and 230 °C, respectively, and the TCR of the rGO/SF sensor was calculated to be 2.20, 1.87, 1.73, 1.66, 1.50, and 1.39%/K for the same reduction temperatures, respectively. The TCR of the rGO and rGO/SF sensors could be tailored by varying the reduction temperature. The TCR of the rGO and rGO/SF sensors obtained in the present study was higher than the values reported in previous studies (Table S1).

The TCR of the rGO sensor was reduced by 20.6, 18.7, 15.6, 7.9, 14.3, and 9.7% for reduction temperatures of 155, 170, 185, 200, 215, and 230 °C when SF layers were added (i.e., for

an rGO/SF sensor), respectively. Although the rGO/SF film had a slightly lower TCR than the rGO film, the TCR of the rGO/SF film resulted in the film showing considerably higher performance as a temperature and humidity sensor (Table S1). The reason for the slightly lower TCR, which is related to the sensor's working mechanism, is discussed later.

The performance of the rGO and rGO/SF sensors as humidity sensors was evaluated by controlling the humidity by using saturated salt solutions (Figure S1b). Figure 6a shows
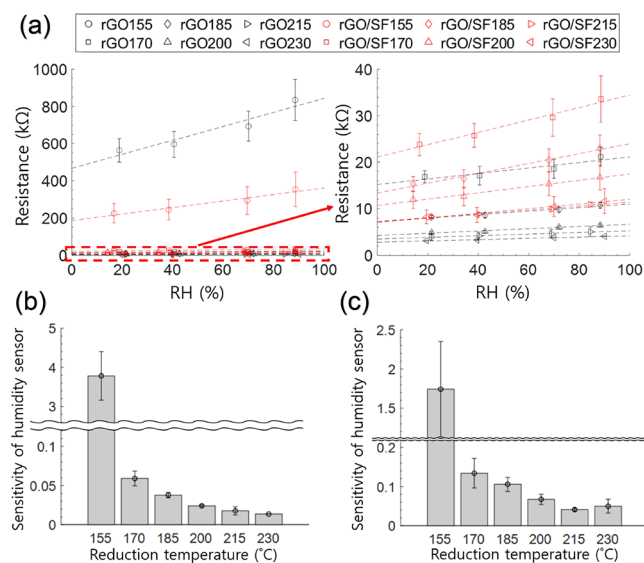

Figure 6. (a) Responsivity of rGO and rGO/SF humidity sensors (fabricated at different reduction temperatures) in terms of resistance change as a function of humidity change, and the gradient of a linear fit to the resistance-RH plot for (b) rGO sensor and (c) rGO/SF sensor.

that the resistance of the rGO and rGO/SF films increased with the relative humidity (11, 33, 75, and 97%). This increase in the resistance indicated the high potential of the films for use as humidity sensors. Furthermore, the slopes in Figure 6a decrease with an increase in the reduction temperature. Since the slopes reflect the sensitivity of the humidity sensor, the sensitivity of the rGO and rGO/SF films can be tailored through an appropriate choice of the reduction temperature (Figure 6b,c). The performance of our humidity sensors was comparable to that of previously reported sensors (Table S2).

For real-time temperature and humidity detection, the response and recovery time are crucial factors. The temperature response and recovery time were measured by moving the rGO/SF sensor between hot plates heated to 25 and 27 °C. The humidity response and recovery time were measured by moving the sensor away from and toward a water-filled container. As shown in Figure S12, the response and recovery time for the temperature change were 5.5 and 5.1 s, respectively, and those for the humidity change were 40 and 45 s, respectively. These values are comparable to previously obtained values presented in Table S2.

The mechanisms of the rGO and rGO/SF films were related to the NTE of rGO and SF (Figure 7a).[40,69,70] In the rGO/SF film, moisture was present between the laminated layers owing to the abundance of hydrophilic surface groups that interacted with water molecules. When the temperature of the sensors increased, water molecules in the laminated layers were
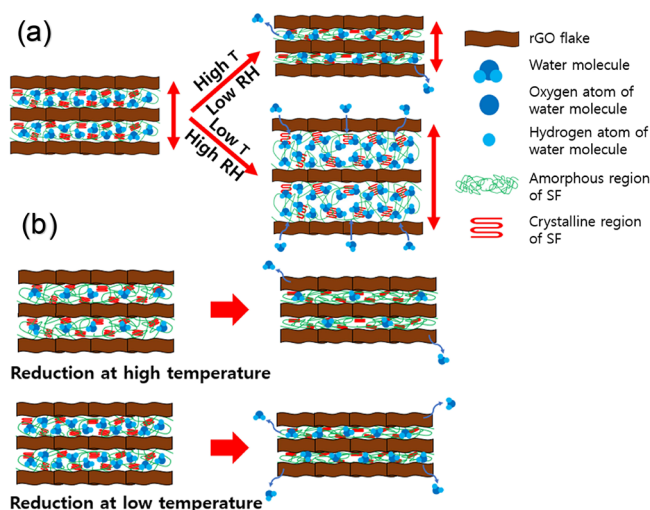
Figure 7. Schematics of (a) mechanism of temperature and humidity sensors and (b) tailorable sensitivity.

desorbed because of debonding between the water molecules and the hydrophilic surface groups of the laminated structure. Moreover, thermally activated hydrogen bonding in SF caused the contraction of β-sheet crystallites, which decreased the thickness of the structure.[69,70] The desorption of water molecules reduced the interval between the laminated layers and thereby enhanced electrical contact between rGO flakes. On the other hand, when the temperature of the sensors decreased, the adsorption of water on the laminated layers led to reduced electrical contact between rGO flakes. Thus, the desorption and adsorption of water induced by changes in the temperature altered the electrical signals of the rGO/SF sensors.

The mechanism of humidity sensors based on the rGO and rGO/SF films was similar to that of the temperature sensors. When the relative humidity decreased or increased, water was desorbed from or adsorbed on rGO and SF, which caused the expansion or contraction of the sensor's structure.[71,72] The swelling of the structure altered the interval between the laminated layers and changed the degree of electrical contact between rGO flakes, which in turn resulted in a change in the electrical signals of the sensors. Thus, the swelling of the sensor structure because of an increase in the relative humidity altered the electrical signals of the rGO and rGO/SF sensors.

The possibility of tailoring the sensitivity of the temperature and humidity sensors by varying the reduction temperature can be explained on the basis of the change in the number of hydrophilic surface functional groups of rGO flakes with the reduction temperature (Figure 7b). For a higher reduction temperature, the deoxidation of rGO flakes was stronger, which reduced the number of hydrophilic groups (Figure 1b,c). This reduction in the number of hydrophilic groups in rGO flakes resulted in a smaller number of water molecules interacting with rGO flakes. Furthermore, the densely formed SF on rGO during the reduction treatment interacted strongly with rGO through hydrogen bonding, which inhibited the interaction between water molecules and rGO.[54,61,62] Because the change in the interval between the laminated layers of the rGO/SF film for a high reduction temperature was less than that for a lower reduction temperature, the electrical signals of sensors were less sensitive to the environment's temperature

and humidity. Accordingly, the sensitivity of the sensors decreased with an increase in the reduction temperature.

The TCR of the rGO sensor decreased when SF was added (i.e., the rGO/SF sensor) (Figure 5b). The hydrophilic groups in rGO flakes bonded with SF through hydrogen bonding, which increased the interfacial shear strength of the sensor.[54,56] In this case, bonding of water molecules with the available hydrophilic groups in rGO flakes could significantly alter the electrical signal of the sensor. Because the hydrophilic groups that had already bonded with SF could not interact with water molecules, the TCR of the rGO/SF sensor was slightly lower than that of the rGO sensor.

The variation of the thickness of the rGO and rGO/SF films with the temperature and relative humidity was investigated using AFM. Dip-coated rGO and rGO/SF films on CA layers were transferred to Si wafers by using sacrificial layers (Section 2.2.2). While the rGO and rGO/SF films were heated by using a heating stage, their edges were scanned with the AFM to measure their thickness (Figure S13). Figure S13 shows representative AFM images of a film (rGO film for a reduction temperature of 155 °C) for different heating stage temperatures.

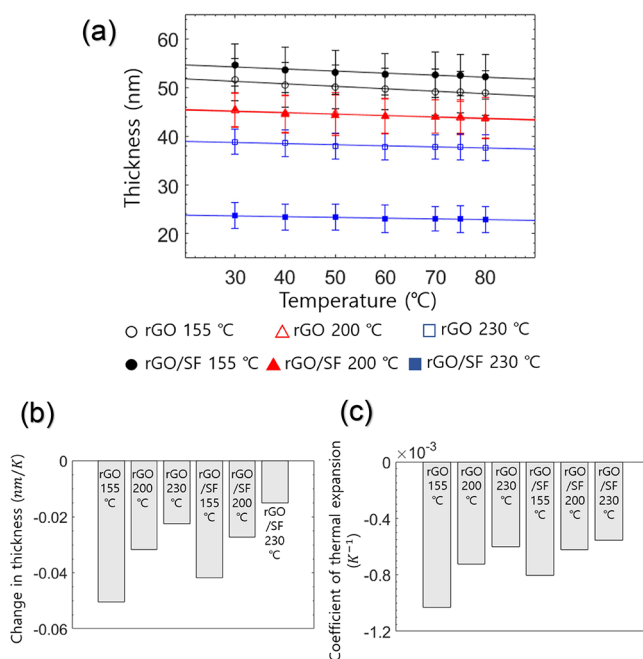Figure 8a shows that the thickness of the rGO and rGO/SF films decreased with an increase in the temperature. The

Figure 8. (a) Thickness of rGO and rGO/SF films at temperatures of 30, 40, 50, 60, 70, 75, and 80 °C for reduction temperatures of 155, 200, and 230 °C. (b) Change in the thickness of the two films for reduction temperatures of 155, 200, and 230 °C. (c) Coefficient of thermal expansion of the two films for reduction temperatures of 155, 200, and 230 °C.

temperature dependence of the thickness resulted from the NTE of the rGO and rGO/SF films and the interaction between water molecules and the laminated structure. The change in the thickness for different reduction temperature is shown in Figure 8b. The change in the thickness of the rGO film for reduction temperatures of 155, 200, and 230 °C was calculated to be −0.050, −0.032, and − 0.023 nm/K, respectively, and the change in the thickness of the rGO/SF

film for these reduction temperatures was calculated to be −0.042, −0.027, and −0.015 nm/K, respectively. The change in the thickness decreased with an increase in the reduction temperature. This decrease resulted from the decrease in the number of hydrophilic functional groups. The reduced number of hydrophilic groups led to reduced interaction between water molecules and the laminated structure, thereby reducing the amount of thickness change. The change in the thickness of the rGO/SF film was smaller than that in the case of the rGO film since the interaction between rGO and water molecules in the former film was hindered by the hydrogen bonding between rGO and SF.

The coefficient of thermal expansion (α) can be expressed as[73]

$$\alpha = \frac{\Delta L/L_0}{L_0 \Delta T} \tag{6}$$

where ΔL is the change in thickness, L_0 is the initial thickness, and ΔT is the change in temperature. The coefficient of thermal expansion of the rGO film for reduction temperatures of 155, 200, and 230 °C was calculated to be −1.03 × 10⁻³, −0.73 × 10⁻³, and −0.60 × 10⁻³/K (Figure 8c), respectively, and that of the rGO/SF film for the same reduction temperatures was calculated to be −0.80 × 10⁻³, −0.62 × 10⁻³, and −0.55 × 10⁻³/K, respectively. The coefficient of thermal expansion of both films decreased with an increase in the reduction temperature, and the decrease is attributed to the reduction in the number of hydrophilic functional groups of rGO flakes, which interact with moisture. Because the thermo-induced thickness change was strongly related to the sensitivity of the sensor, the relationship between the coefficient of thermal expansion and the reduction temperature for the sensors was consistent with that between the sensitivity of the sensors and the reduction temperature.

Reversible thermal expansion was investigated by comparing the thickness of a film before and after heating (Figure S14). The thickness of the film at 30 °C was 45.6 nm, and after being heated to 80 °C, its thickness decreased to 43.6 nm. When the film heated to 80 °C was cooled to 30 °C, its thickness increased to 45.7 nm. Thus, the thickness of the film before being heated to 80 °C was almost identical to that after being heated to 80 °C and cooled, which showed the outstanding reversibility of the film. Because the mechanism of the sensor was based on its electrical signal changing with its thickness, reversible thermal expansion endowed the sensor with reversibility of electrical signals.

To investigate the stability, reliability, and durability of the rGO/SF sensor, we investigated its responsivity (resistance change $\Delta R/R_0$) under repetitive temperature and humidity changes. Figure S15 shows the method used for temperature and humidity cycling. The temperature cycling test was performed repeatedly by heating and cooling the sensors with a heating pad, and the humidity cycling test was conducted using a linear motor with which the sensor could be moved toward and away from water to give rise to repetitive relative humidity changes. The temperature responsivity of the sensor to heat produced by the heating pad was evaluated for 1000 cycles for the temperature range 40−60 °C. The humidity responsivity of the sensor to humidity varied by using the linear motor was evaluated for 1000 cycles for the relative humidity range 50−85%. Figure 9 shows the responsivity of the temperature and humidity sensor for 0,
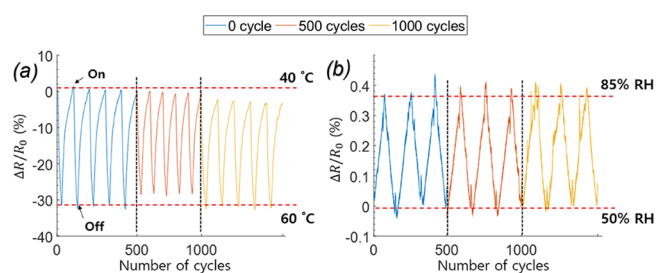

Figure 9. (a) Result of the temperature cycling test for the rGO/SF sensor for a reduction temperature of 170 °C, performed to ascertain the sensor's stability and durability. (b) Result of the humidity cycling test for the humidity sensor, performed to assess the stability and durability of the sensor.

500, and 1000 cycles. The responsivity of the sensor in the cycling tests was nearly unchanged, which indicated high stability, reliability, and durability of the rGO/SF sensor.

The durability of the rGO/SF sensor was higher than that of the rGO sensor. Furthermore, the rGO/SF film had higher mechanical properties, such as elastic bending modulus and flexural rigidity, than the rGO film (Figure 3). The mechanical bending test was performed for the rGO and rGO/SF films, and their surface was monitored during the test with an optical microscope with a 388.5× magnification (Figure 10). Both
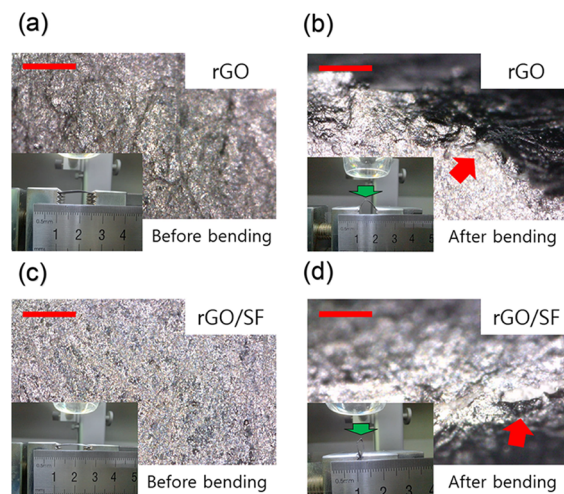

Figure 10. Surface of the rGO sensor (a) before and (b) after the bending test (diameter: 2.1 mm), and the surface of the rGO/SF sensor (c) before and (d) after the bending test (diameter: 0.8 mm). The delamination area is shown by a red arrow. All scale bars are 200 μm.

films were placed on a clamp to apply a bending displacement (Figure 10; inset images). The bending of the films was increased by using the clamp. When the films were bent by the clamp (the mechanical bending test), the region with the smallest bending diameter in the films (Figure 10b,d; a green arrow) was observed with an optical microscope. After the films were delaminated, the bending diameter of the films was measured. While the rGO film was delaminated at a bending diameter of 2.1 mm, the rGO/SF film was delaminated at a bending diameter of 0.8 mm. The delaminated area of the rGO and rGO/SF films is indicated by a red arrow in Figure 10b,d. The mechanical bending test results indicated that failure occurred because of interfacial delamination between the top

and bottom layers. A smaller bending diameter without delamination represented higher interfacial strength between layers, and it indicated high wearability. Thus, the rGO/SF sensor is more suitable than the rGO sensor for use as a wearable sensor. The good wearability of the rGO/SF sensor was attributed to its high interfacial shear strength resulting from strong interaction between the rGO and SF layers.[58,60]

The high durability of the rGO/SF sensor resulted in the sensor showing high stability of electrical signals. The rGO and rGO/SF sensors fabricated with a reduction temperature of 200 °C were repeatably bent 50 times with a displacement of 6 mm and a bending rate of 1 mm/min by using a tensile test machine. While the electrical signal of the rGO sensor changed after being bent 50 times (compared with the electrical signal before the bending test), the rGO/SF sensor withstood repeated bending and its electrical signal was almost unchanged before and after the bending test (Figure 11).
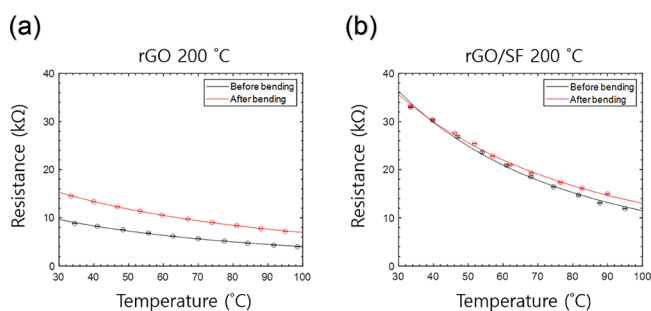

Figure 11. Evaluation of the performance of sensors after the bending test through a comparison with the performance before the bending test: (a) rGO and (b) rGO/SF sensors fabricated with a reduction temperature of 200 °C.

Furthermore, while the rGO sensor was delaminated after repeated bending, the rGO/SF film withstood the bending test (Figure S16). The higher durability of the rGO/SF sensor makes it promising for practical external use as a wearable sensor without failure.

The durable, sensitive, and wearable rGO/SF temperature and humidity sensor can be used as a physiological signal monitoring sensor, such as a respiratory rate sensor. The rGO/SF sensor was attached to the philtrum of a person to detect respiration (Figure 12a; inset image), and it detected the respiratory rate for normal breaths to be 18.7 breaths/min (Figure 12a). The detected breaths were mostly typical of the
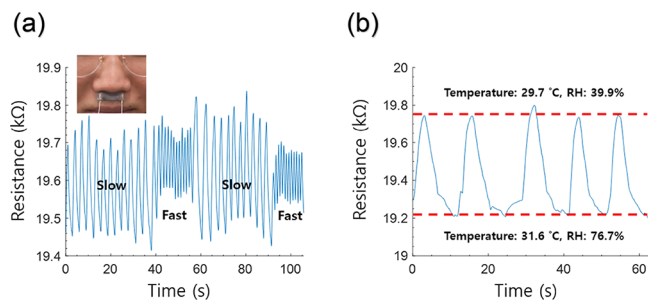

Figure 12. (a) Respiration rates detected by the rGO/SF sensor. (b) Electrical signal of the rGO/SF sensor in the philtrum region induced by the inhaled air (upper red dashed line; temperature of 29.7 °C and relative humidity of 39.9%) and exhaled air (lower red dashed line; temperature of 31.6 °C and relative humidity of 76.7%).

normal healthy state of adults. When the respiratory rate was excessively increased intentionally, the rGO/SF sensor detected a rapid respiration rate of 51.3 breaths/min. It is known that adults with a respiratory rate of over 24 breaths/min are generally diagnosed as being critically ill.[74] It is noteworthy that the proposed rGO/SF sensor could detect a respiratory rate of over 24 breaths/min. Thus, it can be used to provide alerts during emergencies for patients with a critical disease.

The respiration sensing mechanism of the rGO/SF sensor was attributed to respiration-associated changes in the temperature and humidity in the philtrum region (Figure 12b). The temperature and humidity conditions of the philtrum region were altered by the inhaled and exhaled air.[75,76] The temperature and humidity monitored by commercial temperature and humidity sensors in one cycle of inspiration and expiration are between 29.7 °C/39.9% RH and 31.6 °C/76.7% RH (red dashed lines in Figure 12b). It was found that the rGO/SF sensor could detect changes in the temperature and humidity in the philtrum region. The rGO/SF sensors worked properly and continuously monitored changes in the temperature and humidity in the philtrum region during breathing (blue waveform in Figure 12b). It is concluded that the proposed rGO/SF sensor has the potential to be used in the fields of healthcare and biomedical monitoring and in physiological signal monitoring devices.

4. CONCLUSIONS

In this work, a wearable rGO/SF-based temperature and humidity sensor was fabricated using an LbL technique and thermal reduction treatment. The mechanical properties of the rGO/SF film were determined by performing the AFM bending test. Compared with an rGO film, rGO/SF films fabricated with reduction temperatures of 155, 200, and 230 °C showed a bending modulus that was higher by 99.5, 232.6, and 81.5%, respectively. The mechanically reinforced rGO/SF film was characterized by strong interaction between rGO and SF because of SF binding strongly with rGO during recrystallization, and the strong interaction increased the interfacial shear strength of the film's structure. The mechanism of the sensor is attributed to its electrical signal changing in response to absorption/desorption of water molecules onto/from the LbL structure. The sensitivity of the rGO/SF sensor could be tuned by varying the reduction temperature. The TCR of the sensor was adjusted to 2.20, 1.87, 1.73, 1.66, 1.50, and 1.39%/K for reduction temperatures of 155, 170, 185, 200, 215, and 230 °C, respectively. The sensitivity of the humidity sensor decreased with an increase in the reduction temperature. Furthermore, compared with the TCR of the rGO sensor, the TCR of the rGO/SF sensor was slightly degraded by 20.6, 18.7, 15.6, 7.9, 14.3, and 9.7% for reduction temperatures of 155, 170, 185, 200, 215, and 230 °C, respectively. Despite this degradation, the durable rGO/SF sensor showed outstanding robustness against repeatedly applied temperature, humidity, and bending loads, without any performance degradation, unlike the rGO sensor. The rGO/SF temperature and humidity sensor can be used in the fields of healthcare and biomedical monitoring, for instance, as a respiration sensor. The results of this study demonstrate that the rGO/SF temperature and humidity sensor has high potential for use in next-generation wearable devices. Furthermore, the results can serve as a guide for the fabrication of rGO-based devices that can be used in complex environ-

mental conditions. In future work, we intend to develop an rGO/SF sensor with strain-insensitive electrical properties by using origami and kirigami structures for better use in healthcare and human−machine interface applications.

■ ASSOCIATED CONTENT

ⓈⒾ Supporting Information

The Supporting Information is available free of charge at https://pubs.acs.org/doi/10.1021/acs.biomac.3c00106.

> Schematic of the sensor evaluation method, sensor resistance, EDS plots of films, AFM images of films on Cu mesh, force−distance curves, load−deflection plots during approaching and retracting, surface roughness, FTIR spectra, AFM image of films with and without an LbL structure, resistance−temperature curve of sensors, response and recovery curves, specifications and comparison of various wearable temperature and humidity sensors, experimental setup for measuring film thickness at various temperatures, AFM images of films at various temperature, methods for cyclic responsivity measurements of sensors, and film delamination after repeated bending tests (PDF)

■ AUTHOR INFORMATION

Corresponding Author

Sunghan Kim − School of Mechanical Engineering, Chung-Ang University, Seoul 06974, Korea; ◉ orcid.org/0000-0003-0597-5512; Email: sunghankim@cau.ac.kr

Authors

Hyeonho Cho − School of Mechanical Engineering, Chung-Ang University, Seoul 06974, Korea

Chanui Lee − School of Mechanical Engineering, Chung-Ang University, Seoul 06974, Korea

ChaBum Lee − J. Mike Walker '66 Department of Mechanical Engineering, Texas A&M University, College Station, Texas 77843-3123, United States

Sangmin Lee − School of Mechanical Engineering, Chung-Ang University, Seoul 06974, Korea; ◉ orcid.org/0000-0002-6713-4797

Complete contact information is available at:
https://pubs.acs.org/10.1021/acs.biomac.3c00106

Author Contributions

§H.C. and C.L. contributed equally to this work.

Notes

The authors declare no competing financial interest.

■ ACKNOWLEDGMENTS

■ REFERENCES

(1) Choi, J.-H.; Loftness, V. Investigation of human body skin temperatures as a bio-signal to indicate overall thermal sensations. Build. Environ. 2012, 58, 258.

(2) Jiang, Z.; Shi, X.; Qiao, F.; Sun, J.; Hu, Q. Multistimuli-responsive PNIPAM-based double cross-linked conductive hydrogel with self-recovery ability for ionic skin and smart sensor. Biomacromolecules 2022, 23, 5239−5252.

(3) Trung, T.-Q.; Lee, N.-E. Flexible and stretchable physical sensor integrated platforms for wearable human-activity monitoring and personal healthcare. Adv. Mater. 2016, 28, 4338−4372.

(4) Gu, Y.; Hao, J.; Wu, T.; Zhang, Z.; Zhang, Z.; Li, Q. Bimetallic MoNi/WNi nanoalloys for ultra-sensitive wearable temperature sensors. J. Mater. Chem. A 2022, 10, 5402.

(5) Ma, L.; Wu, R.; Patil, A.; Zhu, S.; Meng, Z.; Meng, H.; Hou, C.; Zhang, Y.; Liu, Q.; Yu, R.; Wang, J.; Lin, N.; Liu, X.-Y. Full-textile wireless flexible humidity sensor for human physiological monitoring. Adv. Funct. Mater. 2019, 29, No. 1904549.

(6) Liu, X.; Zhang, D.; Wang, D.; Li, T.; Song, X.; Kang, Z. A humidity sensing and respiratory monitoring system constructed from quartz crystal microbalance sensors based on a chitosan/polypyrrole composite film. J. Mater. Chem. A 2021, 9, 14524.

(7) Zhang, S.; Geryak, R.; Geldmeier, J.; Kim, S.; Tsukruk, V. V. Synthesis, assembly, and applications of hybrid nanostructures for biosensing. Chem. Rev. 2017, 117, 12942.

(8) Danninger, D.; Pruckner, R.; Holzinger, L.; Koeppe, R.; Kaltenbrunner, M. MycelioTronics: Fungal mycelium skin for sustainable electronics. Sci. Adv. 2022, 8, No. eadd7118.

(9) Han, M.; Shen, W. Nacre-inspired cellulose nanofiber/MXene flexible composite film with mechanical robustness for humidity sensing. Carbohydr. Polym. 2022, 298, No. 120109.

(10) Tachibana, S.; Wang, Y. F.; Sekine, T.; Takeda, Y.; Hong, J.; Yoshida, A.; Abe, M.; Miura, R.; Watanabe, Y.; Kumaki, D.; Tokito, S. A printed flexible humidity sensor with high sensitivity and fast response using a cellulose nanofiber/carbon black composite. ACS Appl. Mater. Interfaces 2022, 14, 5721−5728.

(11) Stobinski, L.; Lesiak, B.; Malolepszy, A.; Mazurkiewicz, M.; Mierzwa, B.; Zemek, J.; Jiricek, P.; Bieloshapka, I. Graphene oxide and reduced graphene oxide studied by the XRD, TEM and electron spectroscopy methods. J. Electron Spectrosc. Relat. Phenom. 2014, 195, 145.

(12) Olowojoba, G.-B.; Eslava, S.; Gutierrez, E.-S.; Kinloch, A.-J.; Mattevi, C.; Rocha, V.-G.; Taylor, A.-C. In situ thermally reduced graphene oxide/epoxy composites: Thermal and mechanical properties. Appl. Nanosci. 2016, 6, 1015.

(13) Chen, Q.; Liu, Y.; Gu, K.; Yao, J.; Shao, Z.; Chen, X. Silk-based electrochemical sensor for the detection of glucose in sweat. Biomacromolecules 2022, 23, 3928.

(14) Cho, H.; Lee, H.; Lee, S.; Kim, S. Reduced graphene oxide-based wearable and bio-electrolyte triggered pressure sensor with tunable sensitivity. Ceram. Int. 2021, 47, 17702.

(15) Hu, X.; Xia, X.-X.; Huang, S.-C.; Qian, Z.-G. Development of adhesive and conductive resilin-based hydrogels for wearable sensors. Biomacromolecules 2019, 20, 3283.

(16) Xu, L.; Zhai, H.; Chen, X.; Liu, Y.; Wang, M.; Liu, Z.; Umar, M.; Ji, C.; Chen, Z.; Jin, L.; Liu, Z.; Song, Q.; Yue, P.; Li, Y.; Ye, T.-T. Coolmax/graphene-oxide functionalized textile humidity sensor with ultrafast response for human activities monitoring. Chem. Eng. J. 2021, 412, No. 128639.

(17) Zeng, Y.; Li, T.; Yao, Y.; Li, T.; Hu, L.; Marconnet, A. Thermally conductive reduced graphene oxide thin films for extreme temperature sensors. Adv. Funct. Mater. 2019, 29, No. 1901388.

(18) Ni, Y.; Huang, J.; Li, S.; Dong, X.; Zhu, T.; Cai, W.; Chen, Z.; Lai, Y. Robust superhydrophobic rGO/PPy/PDMS coatings on a polyurethane sponge for underwater pressure and temperature sensing. ACS Appl. Mater. Interfaces 2021, 13, 53271.

(19) Wan, S.; Chen, Y.; Fang, S.; Wang, S.; Xu, Z.; Jiang, L.; Baughman, R. H.; Cheng, Q. High-strength scalable graphene sheets by freezing stretch-induced alignment. Nat. Mater. 2021, 20, 624.

(20) Mao, L.; Park, H.; Soler-Crespo, R. A.; Espinosa, H. D.; Han, T. H.; Nguyen, S. T.; Huang, J. Stiffening of graphene oxide films by soft porous sheets. Nat. Commun. 2019, 10, 3677.

(21) Liang, X.; Zhu, M.; Li, H.; Dou, J.; Jian, M.; Xia, K.; Li, S.; Zhang, Y. Hydrophilic, breathable, and washable graphene decorated textile assisted by silk sericin for integrated multimodal smart wearables. Adv. Funct. Mater. 2022, 32, No. 2200162.

(22) Liang, X.; Li, H.; Dou, J.; Wang, Q.; He, W.; Wang, C.; Li, D.; Lin, J.-M.; Zhang, Y. Stable and biocompatible carbon nanotube ink mediated by silk protein for printed electronics. *Adv. Mater.* **2020**, *32*, No. 2000165.

(23) Li, S.; Zhang, Y.; Liang, X.; Wang, H.; Lu, H.; Zhu, M.; Wang, H.; Zhang, M.; Song, Y.; Zhang, Y. Humidity-sensitive chemoelectric flexible sensors based on metal-air redox reaction for health management. *Nat. Commun.* **2022**, *13*, 5416.

(24) Hu, K.; Gupta, M.-K.; Kulkarni, D.-D.; Tsukruk, V.-V. Ultra-robust graphene oxide-silk fibroin nanocomposite membranes. *Adv. Mater.* **2013**, *25*, 2301.

(25) Xiong, R.; Hu, K.; Zhang, S.; Lu, C.; Tsukruk, V. V. Ultrastrong freestanding graphene oxide nanomembranes with surface-enhanced Raman scattering functionality by solvent-assisted single-component layer-by-layer assembly. *ACS Nano* **2016**, *10*, 6702.

(26) Choi, H. K.; Lee, A.; Park, M.; Lee, D. S.; Bae, S.; Lee, S.-K.; Lee, S. H.; Lee, T.; Kim, T.-W. Hierarchical porous film with layer-by-layer assembly of 2D copper nanosheets for ultimate electromagnetic interference shielding. *ACS Nano* **2021**, *15*, 829.

(27) Huang, L.; Li, C.; Yuan, W.; Shi, G. Strong composite films with layered structures prepared by casting silk fibroin–graphene oxide hydrogels. *Nanoscale* **2013**, *5*, 3780.

(28) Zhao, H.; Yue, Y.; Zhang, Y.; Li, L.; Guo, L. Ternary artificial nacre reinforced by ultrathin amorphous alumina with exceptional mechanical properties. *Adv. Mater.* **2016**, *28*, 2037.

(29) Cheng, Q.; Duan, J.; Zhang, Q.; Jiang, L. Learning from nature: Constructing integrated graphene-based artificial nacre. *ACS Nano* **2015**, *9*, 2231.

(30) Shakil, A.; Kim, S.; Polycarpou, A. A. Creep behavior of graphene oxide, silk fibroin, and cellulose nanocrystal bionanofilms. *Adv. Mater. Interfaces* **2022**, No. 2101640.

(31) Ye, C.; Combs, Z. A.; Calabrese, R.; Dai, H.; Kaplan, D. L.; Tsukruk, V. V. Robust microcapsules with controlled permeability from silk fibroin reinforced with graphene oxide. *Small* **2014**, *10*, 5087.

(32) Xie, W.; Tadepalli, S.; Park, S.-H.; Kazemi-Moridani, A.; Jiang, Q.; Singamaneni, S.; Lee, J.-H. Extreme mechanical behavior of nacre-mimetic graphene-oxide and silk nanocomposites. *Nano Lett.* **2018**, *18*, 987.

(33) Zandiatashbar, A.; Lee, G.-H.; An, S.-J.; Lee, S.; Mathew, N.; Terrones, M.; Hayashi, T.; Picu, C.-R.; Hone, J.; Koratkar, N. Effect of defects on the intrinsic strength and stiffness of graphene. *Nat. Commun.* **2014**, *5*, 3186.

(34) Bai, Y.; Cai, H.; Qiu, X.; Fang, X.; Zheng, J. Effects of graphene reduction degree on thermal oxidative stability of reduced graphene oxide/silicone rubber nanocomposites. *High Perform. Polym.* **2015**, *27*, 997.

(35) Richardson, J.-J.; Björnmalm, M.; Caruso, F. Technology-driven layer-by-layer assembly of nanofilms. *Science* **2015**, *348*, 2491.

(36) Alongi, J.; Carosio, F.; Frache, A.; Malucelli, G. Layer by layer coatings assembled through dipping, vertical or horizontal spray for cotton flame retardancy. *Carbohydr. Polym.* **2013**, *92*, 114.

(37) Trung, T.-Q.; Ramasundaram, S.; Hwang, B.-U.; Lee, N.-E. An all-elastomeric transparent and stretchable temperature sensor for body-attachable wearable electronics. *Adv. Mater.* **2016**, *28*, 502.

(38) Liu, Q.; Tai, H.; Yuan, Z.; Zhou, Y.; Su, Y.; Jiang, Y. A high-performance flexible temperature sensor composed of polyethylenei-mine/reduced graphene oxide bilayer for real-time monitoring. *Adv. Mater. Technol.* **2019**, *4*, No. 1800594.

(39) Sehrawat, P.; Islam, S.-S.; Mishra, P. Reduced graphene oxide based temperature sensor: Extraordinary performance governed by lattice dynamics assisted carrier transport. *Sens. Actuators, B* **2018**, *258*, 424.

(40) Zhu, J.; Andres, C.-M.; Xu, J.; Ramamoorthy, A.; Tsotsis, T.; Kotov, N.-A. Pseudonegative thermal expansion and the state of water in graphene oxide layered assemblies. *ACS Nano* **2012**, *6*, 8357.

(41) Borini, S.; White, R.; Wei, D.; Astley, M.; Haque, S.; Spigone, E.; Harris, N.; Kivioja, J.; Ryhanen, T. Ultrafast graphene oxide humidity sensors. *ACS Nano* **2013**, *7*, 11166.

(42) Adib, M. R.; Lee, Y.; Kondalkar, V. V.; Kim, S.; Lee, K. A highly sensitive and stable rGO: MoS$_2$-based chemiresistive humidity sensor directly insertable to transformer insulating oil analyzed by customized electronic sensor interface. *ACS Sens.* **2021**, *6*, 1012.

(43) Wang, Y.; Zhang, L.; Zhang, Z.; Sun, P.; Chen, H. High-sensitivity wearable and flexible humidity sensor based on graphene oxide/non-woven fabric for respiration monitoring. *Langmuir* **2020**, *36*, 9443.

(44) Jia, G.; Zheng, A.; Wang, X.; Zhang, L.; Li, L.; Li, C.; Zhang, Y.; Cao, L. Flexible, biocompatible and highly conductive MXene-graphene oxide film for smart actuator and humidity sensor. *Sens. Actuators, B* **2021**, *346*, No. 130507.

(45) Jason, N. N.; Ho, M. D.; Cheng, W. Resistive electronic skin. *J. Mater. Chem. C* **2017**, *5*, 5845.

(46) Guan, X.; Hou, Z.; Wu, K.; Zhao, H.; Liu, S.; Fei, T.; Zhang, T. Flexible humidity sensor based on modified cellulose paper. *Sens. Actuators, B* **2021**, *339*, No. 129879.

(47) Jiao, S.; Li, Y.; Li, J.; Abrha, H.; Liu, M.; Cui, J.; Wang, J.; Dai, Y.; Liu, X. Graphene oxide as a versatile platform for emerging hydrovoltaic technology. *J. Mater. Chem. A* **2022**, *10*, 18451.

(48) Joshi, P.; Yadav, R.; Hara, M.; Inoue, T.; Motoyama, Y.; Yoshimura, M. Contribution of B, N-co-doped reduced graphene oxide as a catalyst support to the activity of iridium oxide for oxygen evolution reaction. *J. Mater. Chem. A* **2021**, *9*, 9066.

(49) Hummers, W. S., Jr.; Offeman, R. E. Preparation of graphitic oxide. *J. Am. Chem. Soc.* **1958**, *80*, 1339.

(50) Rockwood, D.-N.; Preda, R.-C.; Yücel, T.; Wang, X.-Q.; Lovett, M.-L.; Kaplan, D.-L. Materials fabrication from Bombyx mori silk fibroin. *Nat. Protoc.* **2011**, *6*, 1612.

(51) Yin, K.; Li, H.; Xia, Y.; Bi, H.; Sun, J.; Liu, Z.; Sun, L. Thermodynamic and kinetic analysis of low temperature thermal reduction of graphene oxide. *Nano−Micro Lett.* **2011**, *3*, 51.

(52) Kim, S.; Geryak, R.-D.; Zhang, S.; Ma, R.; Calabrese, R.; Kaplan, D.-L.; Tsukruk, V.-V. Interfacial shear strength and adhesive behavior of silk ionomer surfaces. *Biomacromolecules* **2017**, *18*, 2876.

(53) Geryak, R.; Quigley, E.; Kim, S.; Korolovych, V. F.; Calabrese, R.; Kaplan, D. L.; Tsukruk, V. V. Tunable interfacial properties in silk ionomer microcapsules with tailored multilayer interactions. *Macro-mol. Biosci.* **2019**, *19*, No. 1800176.

(54) Xiong, R.; Kim, H. S.; Zhang, S.; Kim, S.; Korolovych, V. F.; Ma, R.; Yingling, Y. G.; Lu, C.; Tsukruk, V. V. Template-guided assembly of silk fibroin on cellulose nanofibers for robust nanostructures with ultrafast water transport. *ACS Nano* **2017**, *11*, 12008.

(55) Cranston, E. D.; Eita, M.; Johansson, E.; Netrval, J.; Salajkova, M.; Arwin, H.; Wagberg, L. Determination of Young's modulus for nanofibrillated cellulose multilayer thin films using buckling mechanics. *Biomacromolecules* **2011**, *12*, 961.

(56) Yin, Y.; Hu, K.; Grant, A.-M.; Zhang, Y.; Tsukruk, V.-V. Biopolymeric nanocomposites with enhanced interphases. *Langmuir* **2015**, *31*, 10859.

(57) Cho, H.; Shakil, A.; Polycarpou, A.-A.; Kim, S. Enabling selectively tunable mechanical properties of graphene oxide/silk fibroin/cellulose nanocrystal bionanofilms. *ACS Nano* **2021**, *15*, 19546.

(58) Cho, H.; Lee, J.; Hwang, H.; Hwang, W.; Kim, J.-G.; Kim, S. Mechanical properties of graphene oxide−silk fibroin bionanofilms via nanoindentation experiments and finite element analysis. *Friction* **2022**, *10*, 282.

(59) Kim, S.; Xiong, R.; Tsukruk, V.-V. Probing flexural properties of cellulose nanocrystal−graphene nanomembranes with force spectros-copy and bulging test. *Langmuir* **2016**, *32*, 5383.

(60) Wang, Y.; Ma, R.; Hu, K.; Kim, S.; Fang, G.; Shao, Z.; Tsukruk, V.-V. Dramatic enhancement of graphene oxide/silk nanocomposite membranes: Increasing toughness, strength, and Young's modulus via annealing of interfacial structures. *ACS Appl. Mater. Interfaces* **2016**, *8*, 24962.

(61) Sehrawat, P.; Islam, S.-S.; Mishra, P.; Ahmad, S. Reduced graphene oxide (rGO) based wideband optical sensor and the role of

temperature, defect states and quantum efficiency. *Sci. Rep.* **2018**, *8*, 3537.

(62) Chang, H.; Sun, Z.; Saito, M.; Yuan, Q.; Zhang, H.; Li, J.; Wang, Z.; Fujita, T.; Ding, F.; Zheng, Z.; Yan, F.; Wu, H.; Chen, M.; Ikuhara, Y. Regulating infrared photoresponses in reduced graphene oxide phototransistors by defect and atomic structure control. *ACS Nano* **2013**, *7*, 6310.

(63) Lee, C.; Wei, X.; Kysar, J.-W.; Hone, J. Measurement of the elastic properties and intrinsic strength of monolayer graphene. *Science* **2008**, *321*, 385.

(64) Suk, J. W.; Piner, R.-D.; An, J.; Ruoff, R.-S. Mechanical properties of monolayer graphene oxide. *ACS Nano* **2010**, *4*, 6557.

(65) Magoshi, J.; Magoshi, Y.; Nakamura, S.; Kasai, N.; Kakudo, M. Physical properties and structure of silk. V. Thermal behavior of silk fibroin in the random-coil conformation. *J. Polym. Sci. Polym. Phys.* **1977**, *15*, 1675−1683.

(66) Freddi, G.; Monti, P.; Nagura, M.; Gotoh, Y.; Tsukada, M. Structure and molecular conformation of tussah silk fibroin films: Effect of heat treatment. *J. Polym. Sci., Part B: Polym. Phys.* **1997**, *35*, 841.

(67) Yin, Z.; Hannard, F.; Barthelat, F. Impact-resistant nacre-like transparent materials. *Science* **2019**, *364*, 1260.

(68) Trung, T.-Q.; Le, H.-S.; Dang, T.-M.-L.; Ju, S.; Park, S.-Y.; Lee, N.-E. Freestanding, fiber-based, wearable temperature sensor with tunable thermal index for healthcare monitoring. *Adv. Healthcare Mater.* **2018**, *7*, No. 1800074.

(69) Kim, B.-K.; Kwon, O.-H.; Park, W.-H.; Cho, D. Thermal, mechanical, impact, and water absorption properties of novel silk fibroin fiber reinforced poly (butylene succinate) biocomposites. *Macromol. Res.* **2016**, *24*, 734.

(70) Aksakal, B.; Akdere, Ü.; Günay, S.-D.; Çağın, T.; Taşseven, Ç. Influence of repeating sequence on structural and thermal stability of crystalline domain of Bombyx mori silk fibroin. *Mater. Res. Express* **2019**, *6*, 125356.

(71) Zheng, S.; Tu, Q.; Urban, J.-J.; Li, S.; Mi, B. Swelling of graphene oxide membranes in aqueous solution: Characterization of interlayer spacing and insight into water transport mechanisms. *ACS Nano* **2017**, *11*, 6440.

(72) Lee, M.; Jeon, H.; Kim, S. A highly tunable and fully biocompatible silk nanoplasmonic optical sensor. *Nano Lett.* **2015**, *15*, 3358.

(73) Su, Y.; Wei, H.; Gao, R.; Yang, Z.; Zhang, J.; Zhong, Z.; Zhang, Y. Exceptional negative thermal expansion and viscoelastic properties of graphene oxide paper. *Carbon* **2012**, *50*, 2804.

(74) Cretikos, M.-A.; Bellomo, R.; Hillman, K.; Chen, J.; Finfer, S.; Flabouris, A. Respiratory rate: The neglected vital sign. *Med. J. Aust.* **2008**, *188*, 657.

(75) AL-Khalidi, F.-Q.; Saatchi, R.; Burke, D.; Elphick, H.; Tan, S. Respiration rate monitoring methods: A review. *Pediatr. Pulmonol.* **2011**, *46*, 523.

(76) Pereira, C.-B.; Yu, X.; Goos, T.; Reiss, I.; Orlikowsky, T.; Heimann, K.; Venema, B.; Blazek, V.; Leonhardt, S.; Teichmann, D. Noncontact monitoring of respiratory rate in newborn infants using thermal imaging. *IEEE Trans. Biomed. Eng.* **2018**, *66*, 1105.